Nano Energy 146 (2025) 111516

Contents lists available at ScienceDirect

Nano Energy

journal homepage: www.elsevier.com/locate/nanoen

Bridging solar evaporation and advanced oxidative degradation: A MXene-hydrogel platform for synergistic water treatment

Ying Long [a], Shudi Mao [a], Xin Stella Zhang [a], Yihan Shi [a], An Feng [a], Dawei Su [b,*], Wei Wei [a,*], Bing-Jie Ni [c], Qiang Fu [a,*]

[a] Centre for Technology in Water and Wastewater, School of Civil and Environmental Engineering, University of Technology Sydney, Sydney, NSW 2007, Australia
[b] Applied Chemistry & Environmental Science, School of Science, RMIT University, Melbourne, VIC 3000, Australia
[c] UNSW Water Research Centre, School of Civil and Environmental Engineering, University of New South Wales, Sydney, NSW 2052, Australia

ARTICLE INFO

Keywords:
Water pollution
MXene-based hydrogel
Interfacial solar evaporation
Advanced oxidation process
Synergy effect

ABSTRACT

The escalating global water pollution crisis calls for advanced purification technologies that simultaneously enable energy-efficient water recovery and effective pollutant removal. In this study, we report a mechanically robust double-network hydrogel composed of polyacrylamide, polyvinyl alcohol and MXene, designed for integrated interfacial solar evaporation (ISE) and advanced oxidation processes (AOPs). The incorporation of MXene nanosheets enhances photothermal conversion and promotes efficient solar evaporation, owing to their broadband solar absorption. Remarkably, according to the DFT calculation, upon introducing ammonium persulfate (APS) as an oxidant, MXene facilitates electron transfer under sunlight irradiation, triggering the decomposition of APS and the generation of reactive oxidizing species (ROSs). This synergistic system achieves a high solar evaporation rate of 3.07 $kg \cdot m^{-2} \cdot h^{-1}$ while simultaneously degrading 96.13 % methylene blue dye or 91.70 % antibiotic sulfamethoxazole within 24 h. Outdoor validation demonstrates > 99 % pollutant removal efficiency and excellent cycling stability (~90 % after 10 cycles). This work thus offers a scalable and integrated platform for sustainable water treatment by harmonizing physical separation with chemical decontamination.

1. Introduction

Water pollution is an escalating global issue driven by the ever-increasing discharge of industrial effluents, agricultural runoff, and domestic wastewater [1–4]. Industrial wastewater [5,6] often contains chemically stable and bioaccumulative organic micropollutants, including organic dyes and pharmaceutical residues, which threaten both ecosystems and human health [7–10]. This highlights the urgent need for advanced water purification technologies, which are capable of effectively removing persistent contaminants while minimizing energy consumption. Advanced oxidation processes (AOPs) have been extensively studied as effective treatment methods for organic pollutants [11], owing to their ability to generate highly reactive radicals such as hydroxyl (·OH) and sulfate ($\cdot SO_4^-$) that can mineralize a wide range of contaminants [12]. In particular, persulfate-based AOPs, including those that utilize persulfate reagents, offer strong oxidizing power and relatively stable performance across diverse water conditions [13]. However, conventional AOPs systems often rely on ultraviolet (UV) [14] or thermal activation, or transition metal catalysts [15], which can result in high energy consumption, secondary pollution, or complex operational demands [16–18]. These limitations underscore the need for alternative activation strategies that can be sustainably integrated into modern water treatment platforms.

Addressing freshwater scarcity is another pressing challenge threatening sustainable development [19]. Interfacial solar evaporation (ISE) has emerged as a promising strategy for freshwater production [20], offering low-carbon emissions, ease of deployment, and high solar-to-vapor conversion efficiency [21]. ISE leverages photothermal materials (PTM) to localize light and heat at the air-water interface, thereby minimizing thermal losses and enhancing energy efficiency. Nevertheless, the practical application of ISE remains largely limited to desalination and physical separation processes [22–24], which are ineffective against non-volatile organic pollutants. Recent advances in ISE have primarily focused on single-function designs to enhance photothermal conversion efficiency [25,26], or on dual-function systems that combine desalination with energy generation [27–29]. Although

* Corresponding authors.
E-mail addresses: dawei.su@rmit.edu.au (D. Su), Wei.Wei@uts.edu.au (W. Wei), Qiang.Fu@uts.edu.au (Q. Fu).

https://doi.org/10.1016/j.nanoen.2025.111516
Received 28 July 2025; Received in revised form 17 September 2025; Accepted 6 October 2025
Available online 9 October 2025

several studies have reported ISE-coupled advanced oxidation processes (AOP), such as ISE-persulfate activation, ISE-photocatalysis and ISE-Fenton reactions, for organic pollutant degradation [30–32], most of these approaches rely on the separate introduction of photothermal and catalytic materials, necessitating careful coordination to avoid mutual interference.

MXene, a two-dimensional (2D) transition metal carbide, has attracted increasing attention as a PTM due to its strong broadband light absorption, metallic conductivity, surface hydrophilicity, and tuneable surface terminations (e.g., -OH, -F, =O) [33,34]. These features make it a promising candidate for ISE-based desalination. At the same time, the presence of redox-active transition metal sites (e.g., Ti) enables MXene to activate oxidants such as peroxydisulfate, facilitating AOPs [35,36].

In this study, we present a PAM-PVA-MXene hydrogel that leverages its hydrated 3D network to provide mechanical stability, facilitate water transport, and confine the dispersion of MXene nanosheets. Remarkably, the system relies solely on MXene to achieve a synergistic effect by simultaneously enabling solar-driven evaporation and ammonium persulfate (APS)-mediated pollutant degradation. By integrating ISE and AOPs within a single system, our design overcomes the long-standing trade-off between evaporation performance and purification capacity. Furthermore, the PAM-PVA-MXene hydrogel demonstrates excellent cycling stability, scalability, and high efficiency under real-world conditions, offering a robust and sustainable platform for wastewater treatment and advancing the practical integration of ISE and AOPs technologies.

2. Results and discussion

2.1. Design and fabrication

To construct a hybrid hydrogel for solar-driven water purification, we first synthesized $Ti_3C_2T_x$ MXene by selectively etching the Al atomic layers from Ti_3AlC_2 [37], as shown in Scheme 1**a**. In our protocol, Ti_3AlC_2 powder was treated with a mixture of HCl and LiF to generate in-situ HF, which enabled the removal of Al atoms and initiated the formation of the characteristic layered structure of $Ti_3C_2T_X$. After etching, we employed ultrasonic exfoliation to delaminate the multi-layered product into few-layer MXene nanosheets.

Following MXene treatment, we designed a two-step crosslinking strategy to synthesize the double network PAM-PVA-MXene hydrogel (denoted as $APMX_x$, where subscript x corresponds to the amount of MXene added), as illustrated in Scheme 1**b**. The precursors, including acrylamide (AM), *N,N′*-methylenebisacrylamide (MBAm, covalent crosslinker), lithium phenyl-2,4,6-trimethylbenzoylphosphinate (LAP, photo initiator), polyvinyl alcohol (PVA), and exfoliated MXene nanosheets, were mixed in aqueous solution. Upon UV irradiation, rapid free-radical polymerization of AM and MBAm occurred, yielding the primary PAM network. Thereafter, we immersed the UV-cured hydrogel in a glutaraldehyde (GA)/HCl solution. The aldehyde groups of GA reacted with the hydroxyl groups of PVA to generate acetal bonds, resulting in a chemically stable double network. The fabrication process was carefully designed to preserve the photothermal properties of MXene, while utilizing the flexible 3D PAM-PVA network to facilitate water transport and enhance the accessibility to both pollutants and the oxidizing agent.

2.2. Characterization

The surface morphology and internal microporous structure of the as-prepared MXene and APM_2 hydrogel were examined by SEM and EDS analyses (Fig. S1-S2). As shown in Fig. 1a, the MXene nanosheets exhibit a typical layered and accordion-like structure, indicating successful exfoliation. The inset figure further confirms the thin, sheet-like morphology of individual flakes. Upon integration into the polymeric network, the $APMX_x$ hydrogel exhibits a highly porous 3D structure (Fig. 1c), which facilitates efficient water transport and pollutant diffusion. Elemental mapping was conducted to verify the distribution of the key elements in the composite. The EDS mappings of pristine MXene (Fig. 1b) show uniform distribution of Ti, C, O, and F, consistent with the $Ti_3C_2T_X$ composition [38,39]. The elemental mapping of $APMX_x$ (Fig. 1d) confirms the homogeneous distribution of C, O, Ti, and N atoms, suggesting successful integration of MXene into PAM-PVA double networks.

The crystalline structure of MXene was further characterized by XRD (Fig. 1**e**). The MXene shows a broad peak around 9°, corresponding to the (002) plane, confirming the exfoliated layered structure. The diffraction peaks corresponding to (101), (102) and (105) planes either disappeared or significantly decreased in intensity. This result indicates

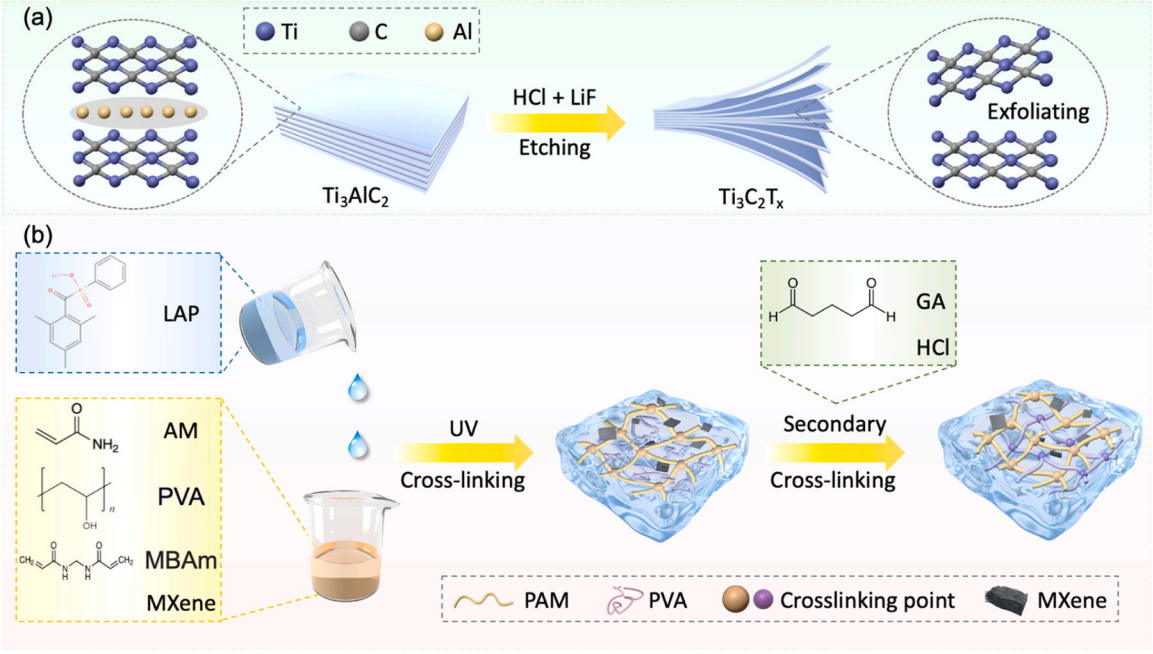

Scheme 1. Preparation process of (a) $Ti_3C_2T_x$ MXene, (b) APMX hydrogel.

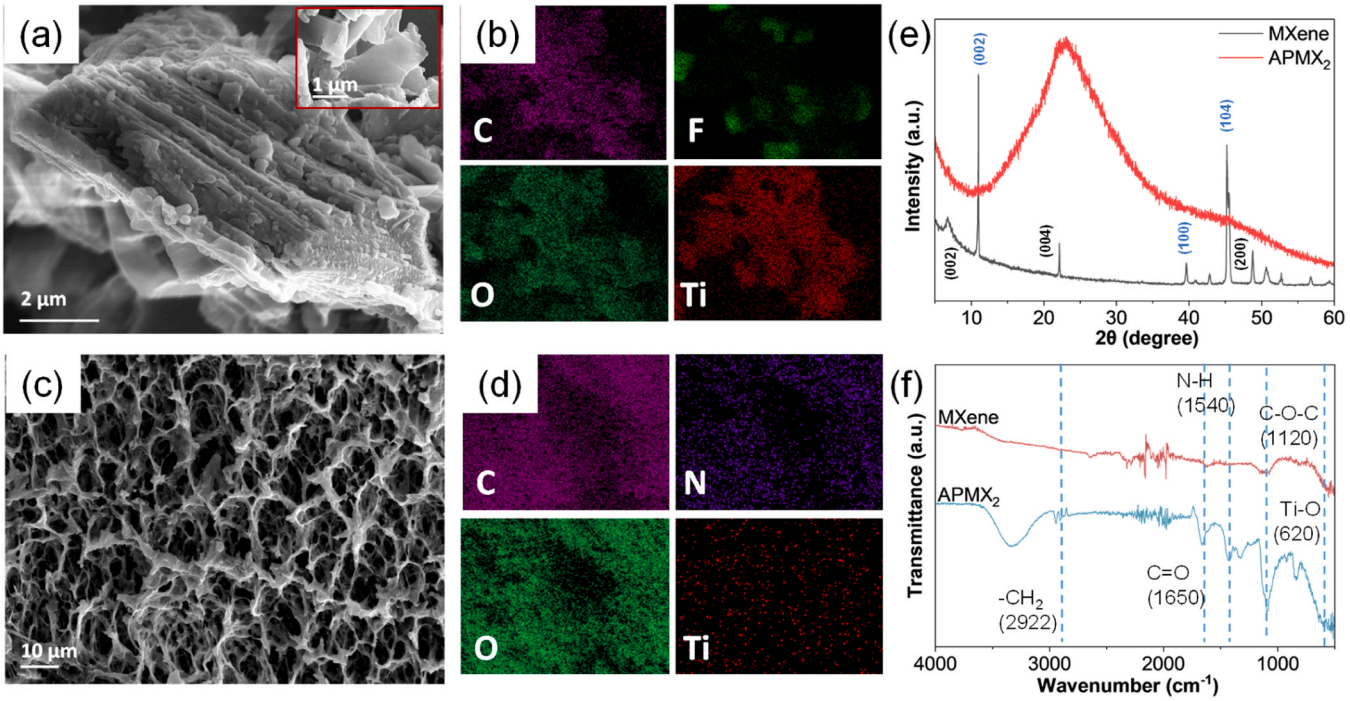

Fig. 1. (a) SEM, and (b) the corresponding elemental mapping (C, O, F, Ti) of the $Ti_3C_2T_x$ MXene. (c) SEM, and (d) the corresponding elemental mapping (C, O, N, Ti) of the hydrogel. (e-f) XRD patterns and FTIR spectra of MXene and $APMX_2$ hydrogel (All XRD analyses are based on Co-Kα radiation).

the etching of the Al layer from the MAX phase. The obvious shift of the (002) peak from ~13° in MAX to ~10.2° in MXene further suggests an increase in interlayer spacing, confirming the successful etching of the MAX phase into MXene [40]. In the case of APM_2, the characteristic peak becomes broader and slightly shifted, indicating strong interfacial interactions and partial intercalation between the polymer network and MXene layers.

To confirm the chemical structures of MXene and the polymeric matrix, FTIR spectra have been performed **(**Fig. S3**,** Fig. 1**f)**. Pristine MXene exhibits characteristic peaks at 620 cm^{-1} and 1120 cm^{-1}, which can be attributed to Ti-O stretching and C-O-C vibration, respectively [41]. In $APMX_x$, new bands appear at 1540 cm^{-1} (N-H bending), 1650 cm^{-1} (C═O stretching), 2922 cm^{-1} (-CH_2 stretching), and -OH stretching at 3253 cm^{-1}[42], confirming the successful preparation of PAM-PVA hydrogels. The shift and intensity changes of key peaks further indicate the formation of strong hydrogen bonding and

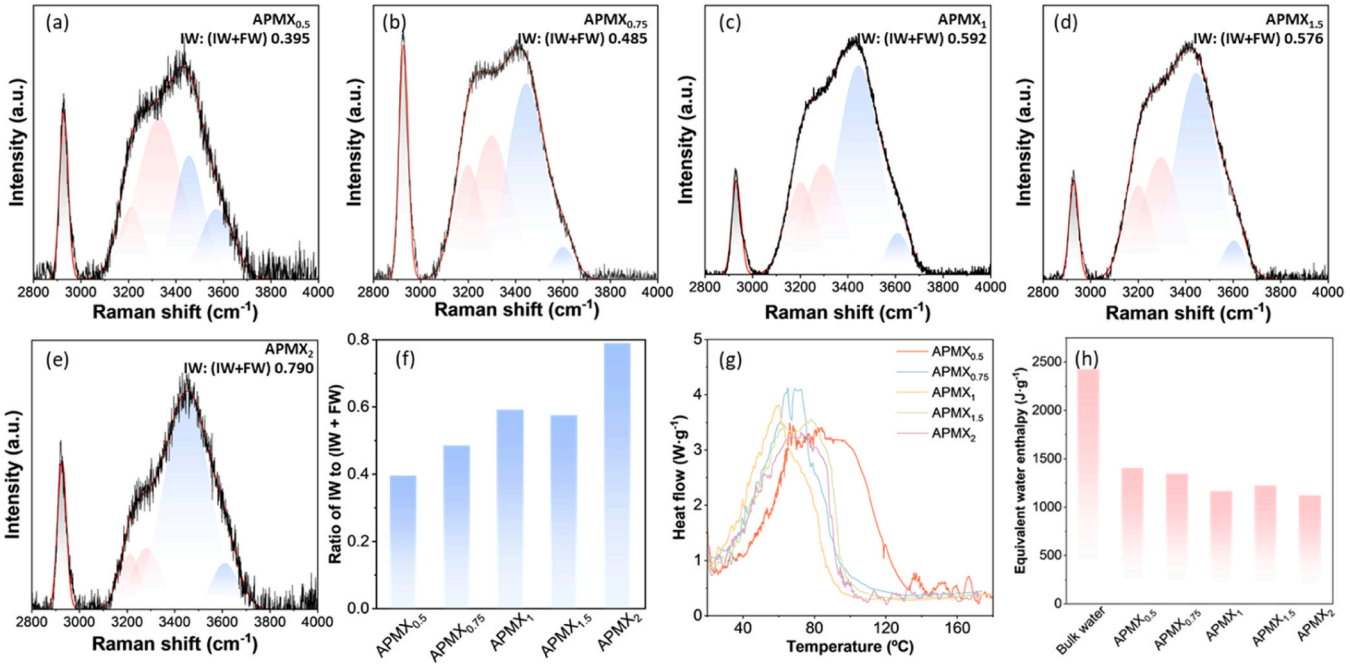

Fig. 2. Fitting curves in the O-H stretching energy region for (a) $APMX_{0.5}$, (b) $APMX_{0.75}$, (c) $APMX_1$, (d) $APMX_{1.5}$, (e) $APMX_2$, (f) The IW: (IW + FW) ratios of all the hydrogels calculated from their Raman spectrum in the O-H stretching energy area, (g) DSC curve of water evaporation processes in hydrogels, (h) The equivalent water vaporization enthalpy of the water in the hydrogels.

coordination interactions between MXene and polymer networks. Collectively, these results confirm the successful fabrication of $APMX_x$, featuring well-dispersed MXene nanosheets embedded within a porous polymeric framework. The strong interfacial interactions and abundant functional groups are expected to promote the formation of intermediate water, as will be discussed in a later section.

Fig. 2**a-f** presents the experimental Raman spectra of the saturated hydrogels ($APMX_x$) with varying MXene content, focusing on the O-H stretching vibration region (~2800–4000 cm^{-1}), along with the corresponding multi-peak fitting results. The spectral fitting employed multiple Gaussian peaks, each representing distinct water populations characterized by differing hydrogen-bonding strengths. Peaks at 3233 cm^{-1} and 3401 cm^{-1} are assigned to relatively strongly hydrogen-bonded water, typically corresponding to free water (FW, pink peaks). In contrast, peaks at 3514 cm^{-1} and 3630 cm^{-1} are attributed to relatively weakly hydrogen-bonded water, corresponding to intermediate water (IW, blue peaks) [43,44]. The relative ratio of intermediate water to free water (IW: FW) was calculated by dividing the integrated area of the IW peaks by that of the FW peaks. Alterations in MXene concentrations from 0.5 to 2 $mg{\cdot}mL^{-1}$ induce changes in both the relative intensity and position of the fitted peaks. Analysis reveals that increasing MXene content significantly reduces the intensity of FW-associated peaks (~3233–3400 cm^{-1}) while enhancing the IW peak intensity (~3514–3630 cm^{-1}). Consequently, the IW/(IW+FW) ratio increases from 0.395 ($APMX_{0.5}$) to 0.79 ($APMX_2$) (Fig. 2**f**). This enhancement is attributed to the increased incorporation of MXene, which introduces additional functional groups that facilitate the formation of intermediate water within the polymer network. It is worth noting that further increasing the MXene content in the PAM-PVA matrix leads to excessive aggregation of MXene nanosheets, resulting in pronounced interfacial incompatibility and a consequent reduction in the mechanical integration of the hydrogel.

The broadening of the endothermic peak in the DSC thermograms reflects the energy heterogeneity arising from the evaporation of multi-state water in the hydrogels (Fig. 2**g**). Thermodynamic analysis confirms that the elevated IW content substantially reduces the equivalent water evaporation enthalpy (ΔH_{vap}), decreasing from 2427 $J{\cdot}g^{-1}$ (pure water reference) to 1117 $J{\cdot}g^{-1}$ (Fig. 2**h**). A strong negative correlation is observed between the IW content and ΔH_{vap} (Fig. 2**f, h**), which can be attributed to the weaker interaction of IW with the polymer matrix, resulting in a lower energy requirement for evaporation and enhanced evaporation performance [45].

2.3. Interfacial solar evaporation performance

Solar-simulated evaporation experiments were conducted using a xenon lamp equipped with an AM 1.5 G filter and an analytical balance for real-time mass loss quantification (Fig. 3**a**). Given that the capture of broadband solar radiation by PTMs directly affects the ISE performance, we characterized the solar absorptivity of APMX hydrogels across varying MXene contents via UV–vis–NIR spectroscopy. As shown in Fig. 3b, these hydrogels exhibit broad-spectrum light absorption across 250–2500 nm, with absorptivity markedly increasing with higher MXene content. To comprehensively assess photothermal response, we monitored real-time temperature distributions of evaporators under simulated sunlight using infrared thermography (Fig. 3**c-d**). Surface and bulk water temperature profiles under one sun irradiation (1 $kW{\cdot}m^{-2}$) are presented in Fig. 3**d**. All hydrogel surfaces exhibited progressive temperature increases, reaching thermal equilibrium within ~ 40 min. $APMX_2$ achieved the highest equilibrium temperature (T_{equ} ~ 36.5°C), followed sequentially by $APMX_{1.5}$ and $APMX_1$, demonstrating enhanced solar-to-thermal conversion efficiency with elevated MXene loading. Bulk water temperatures followed similar trends but remained consistently lower than interfacial temperatures, confirming localized heating at the hydrogel-air interface.

Fig. 3**e** presents the water absorption kinetics of APMX hydrogels with varying MXene content ($APMX_{0.5}$ to $APMX_2$). All samples exhibited rapid initial water uptake, achieving saturation within 200 min. The equilibrium water content decreased with increasing MXene content, with $APMX_{0.5}$ attaining the highest value of 3.52 $g{\cdot}g^{-1}$. Fig. 3**f** compares

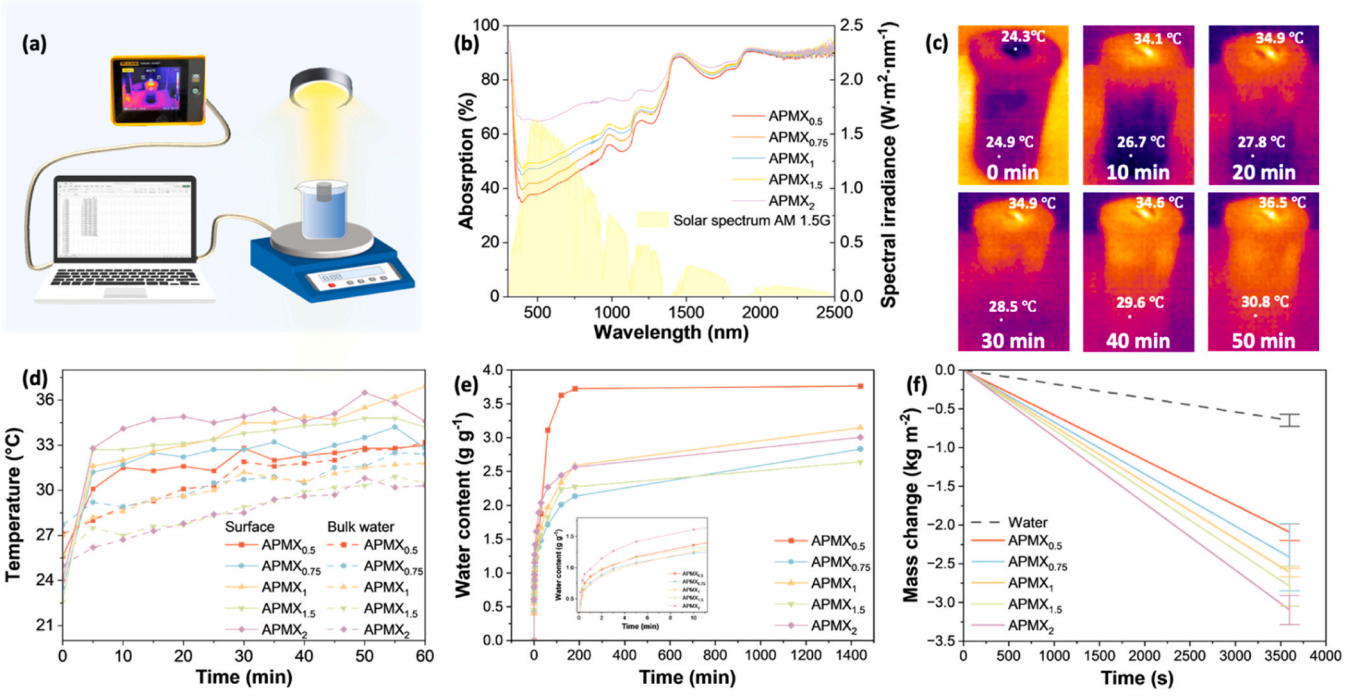

Fig. 3. (a) Schematic illustration of the ISE setup. (b) UV–vis–NIR absorption spectra of the gels with various MXene contents, and the solar spectrum of air mass 1.5 global (AM 1.5 G) with normalised spectral solar irradiance density over the wavelength range of 300–2500 nm. (c) Infrared thermal images under 1 sun illumination. (d) Surface temperature profiles over time under 1 sun. (e) The water content of the gel per gram of the corresponding dry gel is plotted against water absorption time. (f) Water mass changes of different hydrogels and pure water without any gels during the solar vapor generation test under 1 sun irradiation.

the temporal mass loss profiles of various APMX hydrogels and pure water under continuous solar illumination. All hydrogel samples demonstrated significantly enhanced evaporation rates relative to pure water. $APMX_2$ exhibited the most pronounced decline in mass, indicating a superior evaporation rate of 3.07 $kg{\cdot}m^{-2}{\cdot}h^{-1}$. This improved performance primarily arises from the elevated surface temperature, reduced evaporation enthalpy and well-defined water transport pathways established by the incorporation of MXene nanosheets in the hydrogel matrix. To evaluate evaporation performance across different water qualities, $APMX_2$ was tested with fresh water, 10 ppm methylene blue (MB) solution, 10 ppm sulfamethoxazole (SMX) solution, and simulated seawater (Fig. S4). The near-overlapping mass change curves demonstrate stable and consistent evaporation performance regardless of aqueous media. This demonstrates that $APMX_2$ retains its functionalities even in complex environments, confirming its robust performance and practical applicability.

2.4. Degradation performance and mechanism

The adsorption and degradation performance of $APMX_2$ toward organic pollutants in bulk water was evaluated using APS as an oxidizing agent and organic dye MB and antibiotic SMX as representative pollutant models. The advanced oxidation performance of $APMX_2$/APS for pollutant degradation was systematically evaluated, as shown in Fig. 4, with a primary focus on MB and SMX. UV–vis absorption spectra reveal negligible attenuation of the MB peak in the absence of $APMX_2$ or under dark conditions (Fig. 4**a-c**). In contrast, $APMX_2$/APS-mediated AOPs degradation under solar irradiation induces rapid diminution of characteristic MB absorptions (at ~664 nm), achieving near-complete degradation within 24 h. The gradual disappearance of the 664 nm peak, without the emergence of new absorption features, confirms complete mineralization of MB rather than simple decolorization. Visual documentation of MB solution decolorization corroborates these observations (Fig. 4**d**): solutions retain pronounced blue coloration after 24 h under dark conditions, whereas light-exposed samples transition progressively from dark blue to colourless (lower panel). Quantitative degradation kinetics derived from C/C_0 plots demonstrate more than 96.13 % MB decomposition and 91.7 % antibiotic SMX elimination within 24 h under sunlight irradiation, confirming the superior solar-driven AOPs efficiency of $APMX_x$/APS (Fig. 4**e, g**). The results (Fig. S6) show a significant decrease in TOC after treatment, which also confirming the mineralization process. The LC-MS results also indicate that SMX was almost completely decomposed into smaller fragments rather than stable intermediates (Fig. S7). Notably, the effective

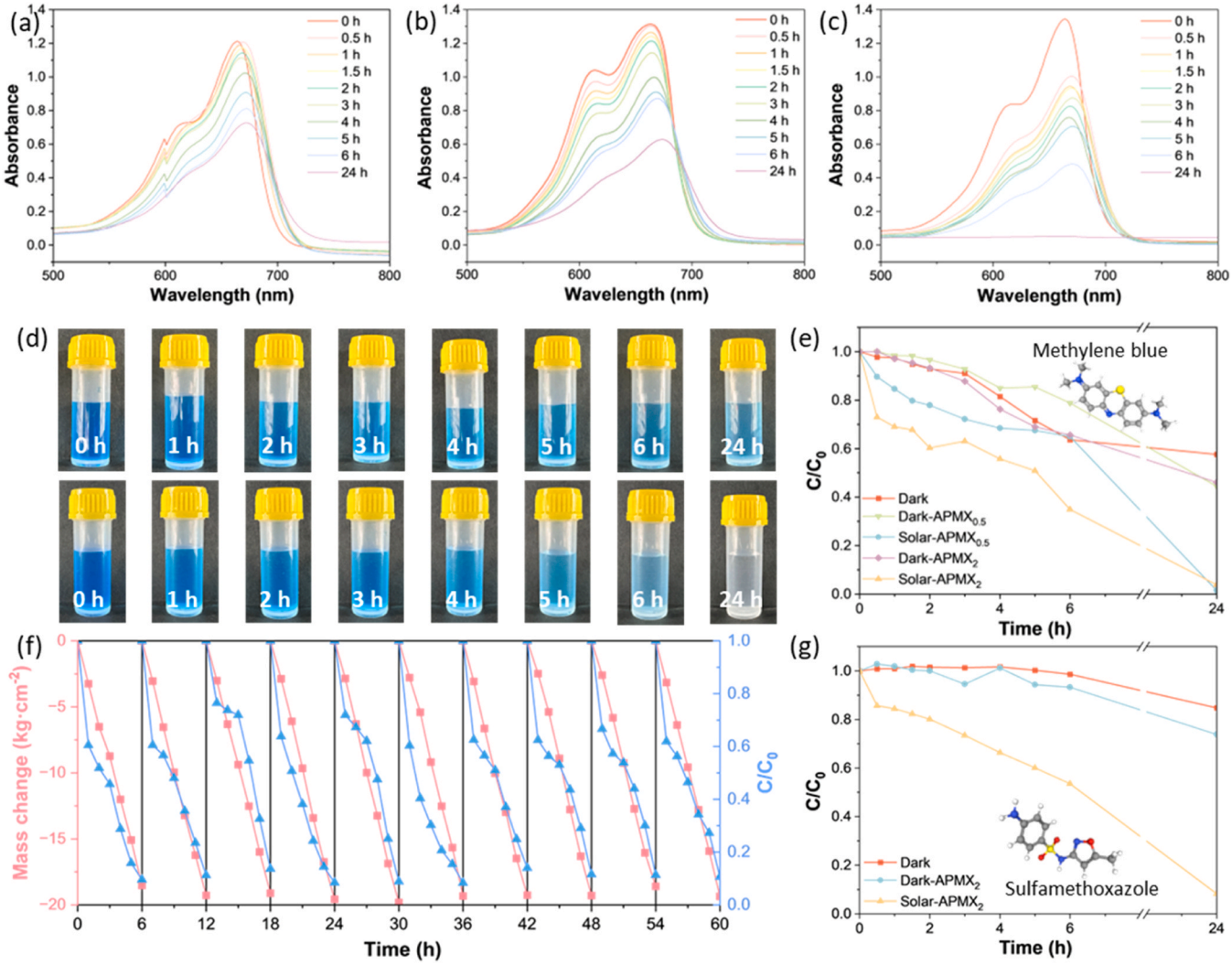

Fig. 4. UV–vis spectra showing the degradation of methylene blue of (a) no hydrogel in the dark, (b) with hydrogel in the dark and (c) with hydrogel under 1 sun over time. (d) The evolution of photodegradation of MB solution under visible-light irradiation. (e) C/C_0 vs time profile indicating degradation efficiency of MB. (f) Recyclability test of the hydrogel for dye degradation over five consecutive cycles under solar illumination. (g) C/C_0 vs time profile indicating degradation efficiency of SMX.

degradation of SMX is of critical environmental significance, as this widely used antibiotic is frequently detected in wastewater and poses serious risks to both aquatic ecosystems and public health [46]. Its persistence and bioactivity contribute to the spread of antibiotic resistance, underscoring the need for energy-efficient removal strategies, such as the synergistic ISE-AOPs approach, to safeguard water quality and mitigate long-term ecological and health impacts.

The cycling stability of $APMX_2$ in both ISE and AOPs is shown in Fig. 4**f.** Over 10 consecutive cycles, $APMX_2$ maintained a stable evaporation rate and consistently high degradation efficiency exceeding 90 %, demonstrating its strong synergistic performance, excellent resistance to photo corrosion, structural integrity, and robust long-term stability (Fig. S11). Collectively, these results establish the practical viability of APMX hydrogels for solar-driven water evaporation and pollutant remediation.

Finally, density functional theory (DFT) simulations were employed to investigate the underlying AOPs mechanisms of APMX/APS system. MXene with 36 Ti and 24 C with the OH termination was modelled as shown in Fig. S9. The APS ($(NH_4)_2(SO_4)_2$) was added above the Ti_3C_2 layer to calculate the energy level at the same vacuum level. The calculated density of state (Fig. S10) indicated that the Fermi level is mainly dominated by the Ti and C from the MXene, while the lower energy level at ~ 0.75 eV is contributed by the $(NH_4)_2(SO_4)_2$. As shown in Fig. 5**a-b**, Wavefunction of the Fermi level and energy level at −0.75 eV are apparently demonstrated by the Ti_3C_2 and $(NH_4)_2(SO_4)_2$, respectively. Therefore, electron transfer from MXene towards $(NH_4)_2(SO_4)_2$ is energetically favorable, as confirmed by the charge density difference plot of the $(NH_4)_2(SO_4)_2$ and MXene (Fig. 5**c**).

To confirm the generation of reactive oxygen species (ROS), 5,5-dimethyl-1-pyrroline-N-oxide (DMPO) was employed as a spin-trapping agent, and electron paramagnetic resonance (EPR) spectroscopy was used to detect the free radicals formed during the decomposition of APS. As shown in Fig. S8, a distinct •OH signal was observed upon the addition of MXene to the APS solution, a weak $SO_4•^-$ signal was also detected, which may be due to the latter being consumed by H_2O [47].

Based on the DFT results and experimental observations, the AOPs reaction mechanism of APMX/APS system is proposed (Fig. 5**d**). The low-valent transition metal active sites (e.g. Ti^{3+}) and structural defects exposed on the MXene surface preferentially adsorb peroxydisulfate ($S_2O_8^{2-}$) in the hydrogel. The $S_2O_8^{2-}$ species withdraws electron density from MXene, facilitating the heterolytic cleavage of the peroxide bond (-O-O-). In this process, Ti^{3+} is oxidized, generating highly reactive sulfate radicals ($SO_4•^-$) along with sulfate ions (1) [48]. The generated $SO_4•^-$ radicals rapidly desorb from the MXene surface and initiate the oxidative degradation of pollutant molecules through electron transfer, hydrogen atom abstraction, or addition reactions, thereby triggering chain oxidation degradation processes. Notably, the highly reactive sulfate radical ($SO_4•^-$) can also react with water molecules to produce another powerful oxidant, hydroxyl radicals (•OH) for oxidation

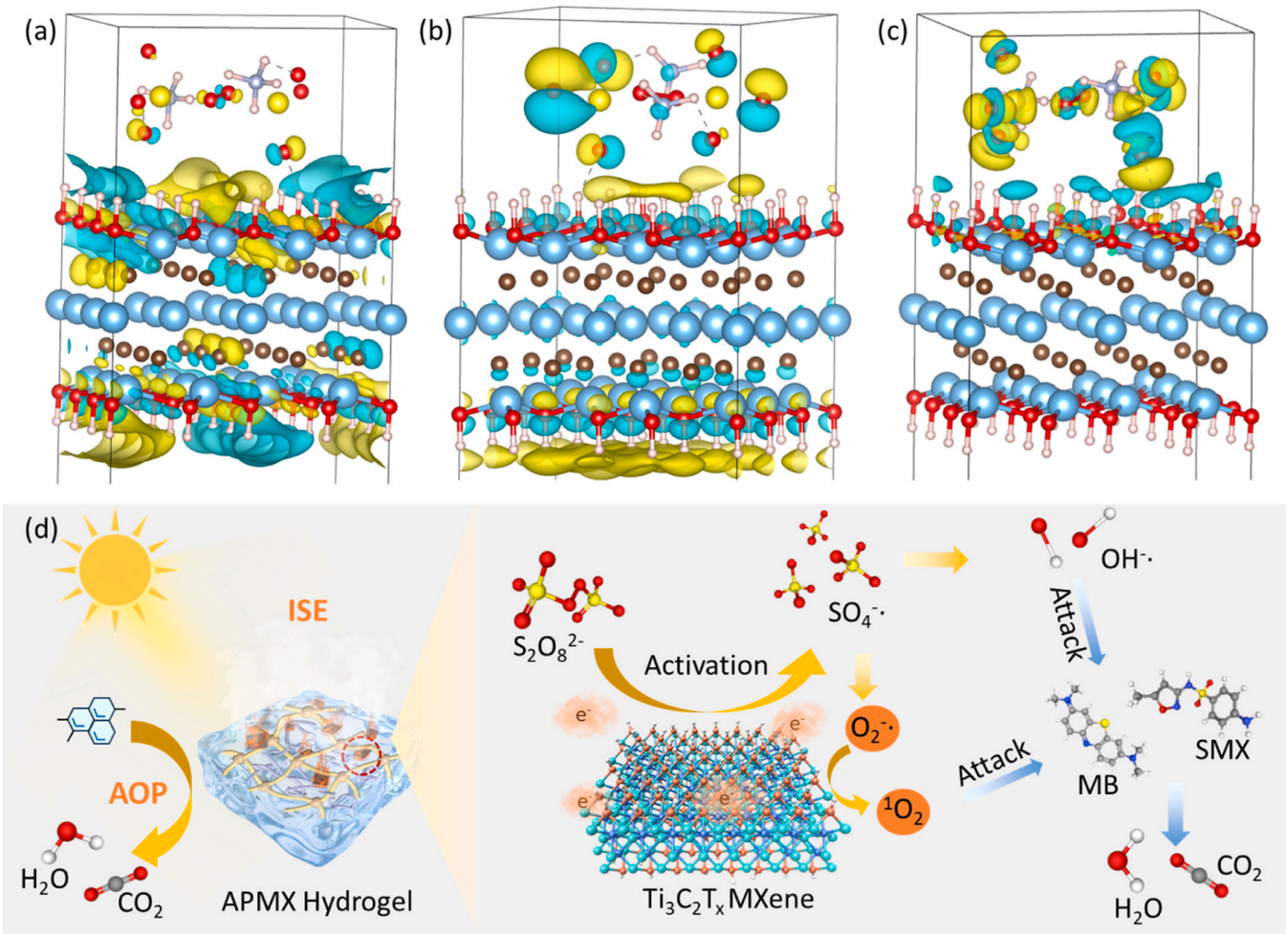

Fig. 5. (a) Wavefunction of the Fermi level, which is dominated by the Ti_3C_2, (b) while the −0.75 eV is contributed by the $(NH_4)_2(SO_4)_2$. (c) Charge density difference between $(NH_4)_2(SO_4)_2$ and MXene. Brown, azure, white, red, yellow, and light grey spheres are C, Ti, H, O, S, and N atoms, respectively. Electron density isosurface = 0.002 |e|/Bohr^3). The colored regions from cyan to yellow represent the loss and gain of electrons, respectively. (d) Proposed mechanism of MXene activating APS for the degradation of MB and SMX.

degradation, along with bisulfate ions (HSO_4^-). This reaction broadens the oxidation capacity of the system by introducing multiple types of reactive oxygen species (ROS) (2) [49]. Additionally, $SO_4\bullet^-$ can engage in non-radical oxidation pathways by reacting with hydroperoxyl radicals (HO_2^-), leading to the formation of singlet oxygen ($^1O_2$) (3) [15]. Finally, this Ti^{3+} regeneration occurs through the reduction of Ti^{4+} by electrons supplied either from the highly conductive MXene substrate itself or from electron-donating organic pollutants (4) [48]. This synergistic radical and non-radical pathway enables efficient and sustainable pollutant degradation, while the regeneration of Ti^{3+} ensures long-term catalytic activity.

$$Ti^{3+} + S_2O_8^{2-} \rightarrow Ti^{4+} + SO_4\bullet^- + SO_4^{2-} \quad (1)$$

$$SO_4\bullet^- + H_2O \rightarrow \bullet OH + HSO_4^- \quad (2)$$

$$SO_4\bullet^- + HO_2^- \rightarrow O_2\bullet^- \rightarrow {}^1O_2 \quad (3)$$

$$Ti^{4+} + e^- \rightarrow Ti^{3+} \quad (4)$$

Overall, this AOPs system operates efficiently under ambient conditions, with the unique electronic structure of MXene facilitating electron transfer for sulfate radical generation and enabling an effective catalytic platform for energy-efficient pollutant removal.

2.5. Real-sunlight validation of the evaporation-oxidation system

Following successful laboratory validation, an outdoor experiment was conducted on 6th May, 2025 (09:00–16:30), to demonstrate the APMX hydrogel's capability for concurrent solar-driven water evaporation and pollutant degradation under natural sunlight. Fig. 6**a** illustrates the experimental configuration under sunlight illumination, integrated with a temperature and humidity monitor to record environmental parameters. As illustrated in Fig. 6**b,** during the experimental period, the environmental temperature fluctuated between 22 and 38°C (red line), relative humidity ranged from 25 % to 60 % R.H. (black line), and solar irradiance varied from 0.0028 to 0.64 kW m^{-2} (blue bars). The $APMX_2$ hydrogel achieves near-complete elimination (98.56 %) of the characteristic MB absorption peak at 664 nm within one daylight period (Fig. 6**c**), confirming the significant oxidation degradation efficacy of APMX/APS. We also quantified the APMX hydrogel's outdoor water evaporation performance. As presented in Fig. 6**d**, we observed an evaporation rate of 11.95 $kg{\cdot}m^{-2}{\cdot}d^{-1}$ and a water collection rate of 6.68 $kg{\cdot}m^{-2}{\cdot}d^{-1}$. The observed discrepancy between these values primarily arises from inherent system closure limitations and condensation efficiency constraints. The collected water samples were further analyzed by UV-Vis spectroscopy, which shows that the distilled water was completely free of dyes, confirming their high quality (Fig. 6**c**). Collectively, these results demonstrate that the $APMX_2$ hydrogel enables efficient, integrated solar water treatment and pollutant purification under real-world conditions, presenting a promising strategy for sustainable water resource management.

3. Conclusions

In conclusion, this work addresses the long-standing trade-off between evaporation efficiency and decontamination capacity in solar-driven water purification by pioneering a MXene-based hydrogel/APS system that synergistically integrates ISE with AOPs technologies. The double-network hydrogel spatially confines both MXene nanosheets and APS oxidants, enabling MXene to function dually as a broadband photothermal converter and an activator that triggers persulfate

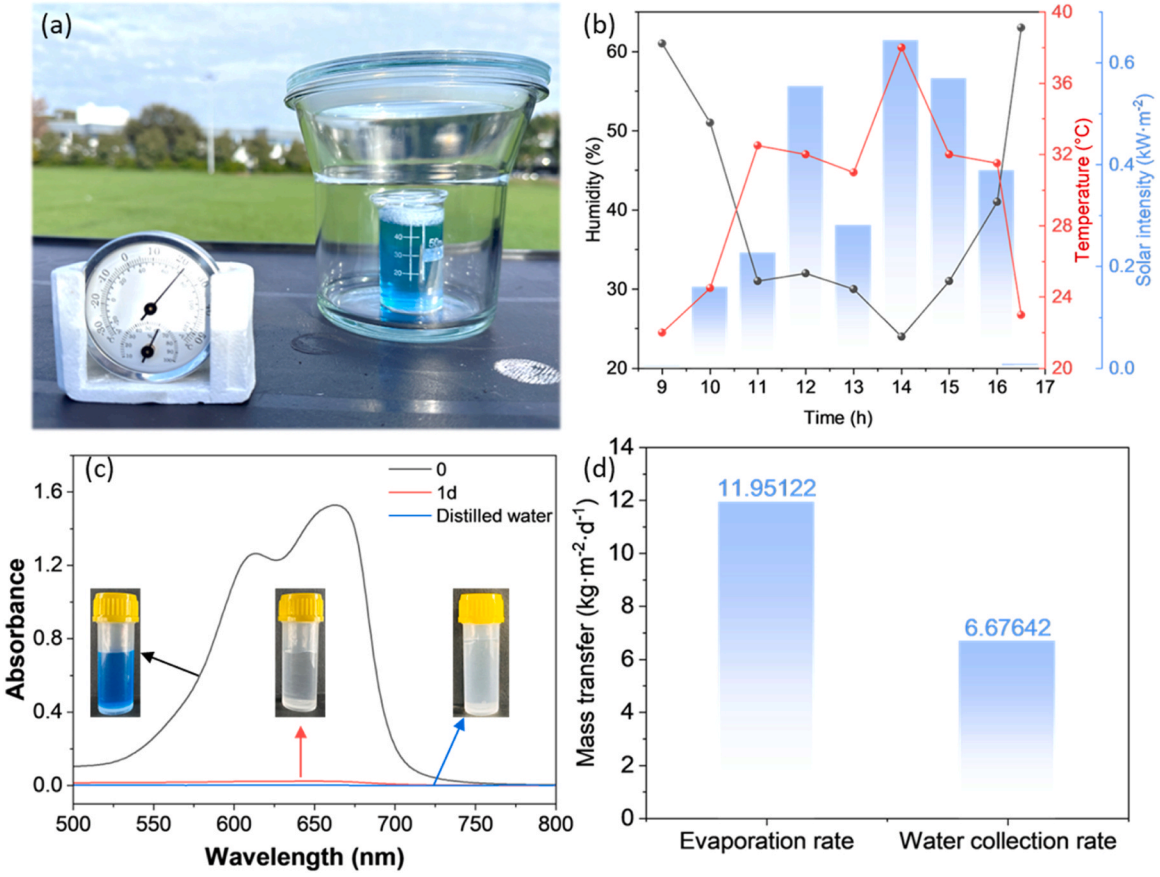

Fig. 6. (a) Photographs of outdoor solar desalination and pollutant degradation. (b) Real-time recording of humidity, temperature, and solar intensity. (c) $APMX_2$ composite hydrogel for MB degradation. (d) Evaporation rate of $APMX_2$ composite hydrogel outdoor tests.

decomposition into sulfate radicals. This dual functionality drives simultaneous solar-driven water evaporation and pollutant mineralization. Crucially, the hydrogel's engineered hydration structure elevates the intermediate water ratio to 79 %, significantly lowering the evaporation enthalpy by 54 %. The APMX system achieves a high outdoor evaporation rate of 11.95 $kg{\cdot}m^{-2}{\cdot}d^{-1}$ and over 98.56 % contaminant degradation under natural sunlight. Simulation studies further validate the proposed AOPs mechanism. With robust reusability (~90 % efficiency over 10 cycles) and strong scalability, this integrated platform establishes a new paradigm for sustainable off-grid wastewater remediation.

4. Experimental section

4.1. Materials

Acrylamide (AM), polyvinyl acetate (PVA, (MW = 89 000–98 000 $g{\cdot}mol^{-1}$), *N*, *N*′-methylenebis(acrylamide) (MBAm), lithium phenyl-2,4,6-trimethyl benzoylphosphinate (LAP), glutaraldehyde solution (GA, 25 wt% in DI water), hydrochloric acid (HCl, 32 wt% in DI water), methylene blue (MB), sulfamethoxazole (SMX), and ammonium persulfate (APS) were purchased from Sigma-Aldrich Australia and used directly without any further purification.

4.2. Synthesis of hydrogels

This double network hydrogel is constructed by photo-crosslinking and chemical crosslinking. In a typical synthesis, 10 g of PVA powder was dissolved in 100 mL of deionized (DI) water at 90 °C for 5 h to obtain a 10 wt% PVA solution. 161.16 mg of AM, 38.84 mg of MBAm, 1 mL of the above PVA solution and different contents of MXene (0.5, 0.75, 1, 1.5, 2 mg) were mixed thoroughly with the help of a vortex mixer. Then 2 mg of LAP powder was added, mixed together and placed under UV light for 10 min to complete crosslinking. The obtained hydrogel was placed in a −20℃ refrigerator and frozen overnight. After that, the frozen hydrogel was thawed naturally and then immersed in a solution containing 3 vol% GA and 0.5 vol% HCl for 30 min for secondary crosslinking, and then the process was repeated twice. The hydrogel was washed with deionized water again to remove all residues. The resulting hydrogel was frozen at −20℃ overnight and freeze-dried to obtain a pure PAM-PVA-MXene ($APMX_x$) hydrogel. Prior to the solar vapor generation test, all samples were fully saturated in deionized water.

4.3. Characterization

A scanning electron microscope (SEM, 10—30 kV) can be used to observe the microscopic morphology of the material surface. Energy dispersive spectroscopy (EDS) spectra were obtained using an energy-dispersive spectroscopy detector. X-ray diffraction (XRD) patterns were recorded using a XRD-Empyrean II (Co). Functional groups of the hydrogels are studied using Raman (Renishaw Raman spectroscopy) and FTIR (Shimadzu MIRacle 10 FT-IR). Measurements were performed at room temperature in the FTIR wavenumber range of 500–2500 cm^{-1} with 64 scans at a resolution of 4 cm^{-1}. Raman spectroscopy was performed in the wavenumber range of 2800–4000 cm^{-1}. A Netzsch DSC 300 Caliris can be used to track the heat change of hydrogels from room temperature to 200 °C at a heating rate of $5°C{\cdot}min^{-1}$. A PerkinElmer Lambda 950 UV-Vis-NIR spectrophotometer was used to record UV-Vis-NIR absorption spectra from 300 to 2500 nm. Measure the absorbance of MB and SMX in the solution using a UV-1900i spectrophotometer. The total organic carbon (TOC) analyzer (Shimatzu TOC-L analyser) was used to measure the TOC values before and after degradation, while liquid chromatography–mass spectrometry (Shimadzu LCMS-8060) was employed to identify the degradation products of SMX. EPR measurements were performed on a Bruker EMX X-Band ESR spectrometer to detect short-lived radical species using the spin trap DMPO.

4.4. Interfacial solar evaporation tests

Solar radiation was simulated using a solar simulator (NBeT HSX-F3000 Xenon light source). A portable power and energy meter console with thermal power sensors (PM100D and S405C, Thorlabs, Germany) calibrated the solar irradiance on the hydrogel surface to one sun (1 $kW{\cdot}m^{-2}$). The hydrogel was secured to floating EPE foam above a beaker of deionized water or simulated wastewater. Parafilm sealed small gaps between the foam and the beaker to minimize water evaporation. An electronic balance (OHAUS Pioneer IC-PX 124) measured water mass loss during the ISE test. Another EPE foam layer insulated the balance from the beaker's heat transfer. Linear regression on the mass loss data determined the evaporation rate. The evaporation rate of pure water is obtained by testing the mass change of a beaker containing water under the same conditions. The evaporation area is calculated according to the diameter of the beaker. A Fluke PTi120 thermal imager recorded hydrogel surface and bulk water temperatures every 5 min during solar steam generation testing.

4.5. Wastewater purification tests

This study investigated the wastewater purification capabilities of an evaporator using MB and SMX as target pollutants. The photocatalytic activity of various hydrogel samples was assessed by measuring changes in absorbance. The experiment involved placing hydrogel in a beaker of simulated wastewater (50 mL, 10 ppm), adding APS, and allowing it to sit in the dark for 30 min to reach adsorption-desorption equilibrium. Photocatalytic advanced oxidation degradation was then initiated using a solar simulator. Samples were taken every 0.5 h or 1 h, filtered (0.22 μm), and analysed using UV-Vis spectrophotometry to measure absorbance at the maximum absorption wavelength. The absorbance ratio (C_t/C_0) was used to evaluate the photocatalytic degradation efficiency.

4.6. Theoretical calculations

The static DFT calculation was performed through the Vienna Ab initio Simulation Package (VASP) [50–53] based on the generalised gradient approximation (GGA) with the Perdew-Burke-Ernzerhof (PBE) [54] function as the exchange-correlation energy function. We used the projector augmented wave potentials with a cutoff energy of 450 eV [55]. The conjugate gradient scheme optimises the atom coordinates until the force is less than 0.01 eV $Å^{-1}$. The $3 \times 3 \times 1$ of k-points were given for Monkhorst-Pack BZ calculations to achieve energy convergence. Meanwhile, the D3 correction was applied for all the layer structure calculations to consider the Van der Waals effect.

CRediT authorship contribution statement

Bing-Jie Ni: Writing – review & editing, Resources, Funding acquisition. **Ying Long:** Writing – original draft, Visualization, Investigation, Formal analysis, Data curation. **Qiang Fu:** Writing – review & editing, Supervision, Methodology, Funding acquisition, Conceptualization. **An Feng:** Visualization, Resources, Investigation. **Yihan Shi:** Visualization, Resources, Investigation. **Xin Stella Zhang:** Visualization, Resources, Investigation. **Shudi Mao:** Visualization, Resources, Investigation. **Wei Wei:** Writing – review & editing, Resources, Funding acquisition. **Dawei Su:** Formal analysis.

Declaration of Competing Interest

The authors declare that they have no known competing financial interests or personal relationships that could have appeared to influence the work reported in this paper.

Acknowledgments

Dr. Wei Wei acknowledges support from the Australian Research Council (ARC) under project DE220100530. Prof. Bing-Jie Ni acknowledges support from the ARC under projects LP240100542 and LP240200633. A/Prof. Qiang Fu acknowledges support from the ARC through the Future Fellowship (FT180100312) and the Discovery Project (DP250102613). Ying Long is supported by the Australian Government Research Training Program (RTP) Scholarship.

Appendix A. Supporting information

Supplementary data associated with this article can be found in the online version at doi:10.1016/j.nanoen.2025.111516.

Data availability

The data that has been used is confidential.

References

[1] Y. Wen, G. Schoups, N. van de Giesen, Organic pollution of rivers: combined threats of urbanization, livestock farming and global climate change, Sci. Rep. 7 (1) (2017) 43289.
[2] Y. Long, et al., Evaluating the spatial and temporal distribution of emerging contaminants in the pearl river basin for regulating purposes, Ecotoxicol. Environ. Saf. 257 (2023) 114918.
[3] Z. Wang, et al., Wastewater surveillance for antibiotics and resistance genes in a river catchment: spatiotemporal variations and the main drivers, Water Res. 251 (2024) 121090.
[4] N. Morin-Crini, et al., Worldwide cases of water pollution by emerging contaminants: a review, Environ. Chem. Lett. 20 (4) (2022) 2311–2338.
[5] E.M. Abd El-Monaem, et al., A comprehensive review on LDH-based catalysts to activate persulfates for the degradation of organic pollutants, npj Clean. Water 6 (1) (2023) 34.
[6] J. Sharma, et al., Pharmaceutical residues: one of the significant problems in achieving 'clean water for all' and its solution, Environ. Res. 215 (2022) 114219.
[7] L. Lin, et al., rGO/Ti3C2 MXene synergistic spontaneous realization of efficient clean water production and pollutant degradation, Desalination 603 (2025) 118657.
[8] B. Mohan, et al., Covalent organic frameworks (COFs) and metal–organic frameworks (MOFs) as electrochemical sensors for the efficient detection of pharmaceutical residues, Environ. Int. 175 (2023) 107928.
[9] H. Gomaa, et al., Efficient removal of noxious methylene blue and crystal violet dyes at neutral conditions by reusable montmorillonite/NiFe2O4@amine-functionalized chitosan composite, Sci. Rep. 12 (1) (2022) 15499.
[10] M. Hu, et al., Construction of Z-scheme heterojunction ZIF-8-decorated ZnO/SiO2 for enhanced visible-light photocatalytic removal of organic pollutants and reduction of cr (VI), Appl. Surf. Sci. 665 (2024) 160321.
[11] D.B. Miklos, et al., Evaluation of advanced oxidation processes for water and wastewater treatment – a critical review, Water Res. 139 (2018) 118–131.
[12] W. Yang, et al., Co-generation of hydroxyl and sulfate radicals via homogeneous and heterogeneous bi-catalysis with the EO-PS-EF tri-coupling system for efficient removal of refractory organic pollutants, Water Res. 243 (2023) 120312.
[13] J. Lee, U. von Gunten, J.-H. Kim, Persulfate-Based advanced oxidation: critical assessment of opportunities and roadblocks, Environ. Sci. Technol. 54 (6) (2020) 3064–3081.
[14] J. Jang, et al., Magnetic Ti3C2Tx (Mxene) for diclofenac degradation via the ultraviolet/chlorine advanced oxidation process, Environ. Res. 182 (2020) 108990.
[15] X. Chen, et al., Degradation of bisphenol a in an oxidation system constructed from Mo2C MXene and peroxymonosulfate, npj Clean. Water 5 (1) (2022) 66.
[16] W. Song, et al., Insight into homogeneous activation of sodium hypochlorite by dithionite coupled with dissolved oxygen (DO@NaClO/DTN) for carbamazepine degradation, Water Res. 277 (2025) 123312.
[17] M. Li, et al., Electrical energy consumption of multiscale UV-AOP reactors for micropollutant removal in drinking water: facilitated prediction by reaction rate constants measured on a Mini-Fluidic photoreaction system, Environ. Sci. Technol. 57 (47) (2023) 18960–18969.
[18] M. Hu, et al., Enhanced peroxymonosulfate activation for antibiotic and heavy metal removal using ZIF-67-derived magnetic Ni/Co-LDH@NC: bimetallic electronic synergy and oxygen vacancy effects, Appl. Catal. B Environ. Energy 362 (2025) 124753.
[19] Y. Liang, et al., Recent innovations in 3D solar evaporators and their functionalities, Sci. Bull. 69 (22) (2024) 3590–3617.
[20] H. Yu, et al., Making interfacial solar evaporation of seawater faster than fresh water, Adv. Mater. 36 (52) (2024) 2414045.
[21] P. Tao, et al., Solar-driven interfacial evaporation, Nat. Energy 3 (12) (2018) 1031–1041.
[22] Y. Ko, et al., Nanocellulose-Based interfacial solar evaporator: integrating sustainable materials and Micro-/Nano-Architectures for solar desalination, Adv. Funct. Mater. 35 (5) (2025) 2414576.
[23] Y. Pan, et al., Simple design of a porous solar evaporator for Salt-Free desalination and rapid evaporation, Environ. Sci. Technol. 56 (16) (2022) 11818–11826.
[24] Q. Xiong, et al., Unlocking zero liquid discharge: a parallel water supply strategy to realize selective salt crystallization for Long-Term interfacial solar evaporation, Adv. Funct. Mater. 35 (7) (2025) 2409257.
[25] H. Tahzibi, S. Azizian, Efficient interfacial solar evaporation using a novel carbonized foam as photo-thermal converter, Sep. Purif. Technol. 354 (2025) 129477.
[26] M.S. Irshad, et al., Advances of 2D-Enabled photothermal materials in hybrid Solar-Driven interfacial evaporation systems toward Water-Fuel-Energy crisis, Adv. Funct. Mater. 33 (51) (2023) 2304936.
[27] X. Jing, et al., Hydrogel solar evaporator with a sodium sulfonate electrolyte backbone enabling continuous high-salinity desalination and energy generation, Nano Energy 142 (2025) 111182.
[28] L. Li, et al., Polyelectrolyte Hydrogel-Functionalized photothermal sponge enables simultaneously continuous solar desalination and electricity generation without salt accumulation, Adv. Mater. 36 (25) (2024) 2401171.
[29] P. Dutta, et al., Electric field guided fast and oriented assembly of MXene into scalable pristine hydrogels for customized energy storage and water evaporation applications, Adv. Funct. Mater. 32 (47) (2022) 2204622.
[30] Y. Song, et al., Solar-driven interfacial evaporation technologies for food, energy and water, Nat. Rev. Clean. Technol. 1 (1) (2025) 55–74.
[31] Y. Guo, et al., Hydrogels and Hydrogel-Derived materials for energy and water sustainability, Chem. Rev. 120 (15) (2020) 7642–7707.
[32] W. Bai, et al., Advanced solar-driven hydrogel sponge for efficient heavy metal wastewater purification and clean water production through interfacial evaporation, Environ. Res. 264 (2025) 120322.
[33] W. Zeng, et al., MXene for photocatalysis and photothermal conversion: synthesis, physicochemical properties, and applications, Coord. Chem. Rev. 508 (2024) 215753.
[34] F. Cao, et al., Recent advances in oxidation stable chemistry of 2D MXenes, Adv. Mater. 34 (13) (2022) 2107554.
[35] M. Ding, et al., MXene-based catalysts for water purification in the persulfate-based Fenton-like system, J. Water Process Eng. 77 (2025) 108291.
[36] X. Wu, et al., Interfacial solar evaporation: from fundamental research to applications, Adv. Mater. 36 (23) (2024) 2313090.
[37] Y. Zhu, et al., Emerging MXene-based catalysts for advanced oxidation processes, Fuel 392 (2025) 134859.
[38] P. Yasaei, et al., Mapping hot spots at heterogeneities of Few-Layer Ti3C2 MXene sheets, ACS Nano 13 (3) (2019) 3301–3309.
[39] S. Mushtaq, et al., MXene/AgNW composite material for selective and efficient removal of radioactive cesium and iodine from water, Sci. Rep. 13 (1) (2023) 19696.
[40] M. Alhabeb, et al., Guidelines for synthesis and processing of Two-Dimensional titanium carbide (Ti3C2Tx MXene), Chem. Mater. 29 (18) (2017) 7633–7644.
[41] A.R. Khan, et al., Two-dimensional transition metal carbide (Ti3C2Tx) as an efficient adsorbent to remove cesium (Cs+), Dalton Trans. 48 (31) (2019) 11803–11812.
[42] S. Sreeja, et al., Organic dye impregnated poly(vinyl alcohol) nanocomposite as an efficient optical limiter: structure, morphology and photophysical properties, J. Mater. Chem. C. 1 (24) (2013) 3851–3861.
[43] B. Fu, et al., Multi-shelled hollow porous carbon nanospheres-based evaporator for highly efficient solar-driven desalination, Nano Energy 129 (2024) 110054.
[44] S. Mao, et al., Investigation of structure–property–application relationships of a hydrogel-based solar vapor generator, J. Mater. Chem. A 11 (42) (2023) 23062–23070.
[45] Y. Wang, et al., Boosting efficient ammonium rejection and water evaporation rate by Solar-Driven hydrogel evaporation, Adv. Energy Sustain. Res. 5 (8) (2024) 2400047.
[46] H. Zhang, et al., Comprehensive assessment of toxicity and environmental risk associated with sulfamethoxazole biodegradation in sulfur-mediated biological wastewater treatment, Water Res. 246 (2023) 120753.
[47] W. Zhang, et al., MXene triggered free radical polymerization in Minutes toward All-Printed Zn-Ion hybrid capacitors and beyond, Angew. Chem. Int. Ed. 64 (1) (2025) e202413728.
[48] P. Eghbali, et al., Recent advances in design and engineering of MXene-based catalysts for photocatalysis and persulfate-based advanced oxidation processes: a state-of-the-art review, Chem. Eng. J. 480 (2024) 147920.
[49] F. Wang, et al., Fluorine-free MXene activate peroxymonosulfate to remove tetracyclic antibiotics, Sep. Purif. Technol. 314 (2023) 123549.
[50] G. Kresse, J. Hafner, Ab initio molecular dynamics for liquid metals, Phys. Rev. B 47 (1) (1993) 558.

[51] G. Kresse, J. Hafner, Ab initio molecular-dynamics simulation of the liquid-metal–amorphous-semiconductor transition in germanium, Phys. Rev. B 49 (20) (1994) 14251.
[52] G. Kresse, J. Furthmüller, Efficiency of ab-initio total energy calculations for metals and semiconductors using a plane-wave basis set, Comput. Mater. Sci. 6 (1) (1996) 15–50.
[53] G. Kresse, J. Furthmüller, Efficient iterative schemes for ab initio total-energy calculations using a plane-wave basis set, Phys. Rev. B 54 (16) (1996) 11169.
[54] J.P. Perdew, M. Ernzerhof, K. Burke, Rationale for mixing exact exchange with density functional approximations, J. Chem. Phys. 105 (22) (1996) 9982–9985.
[55] P.E. Blöchl, Projector augmented-wave method, Phys. Rev. B 50 (24) (1994) 17953.